1 # Slow build-up of turbidity currents triggered by a moderate

2 # earthquake in the Sea of Marmara

4 Pierre Henry[1], M Sinan Özeren[2], Nurettin Yakupoğlu[3], Ziyadin Çakir[3], Emmanuel de

5 Saint-Léger[4], Olivier Desprez de Gésincourt[4], Anders Tengberg[5], Cristele Chevalier[6],

6 Christos Papoutsellis[1], Nazmi Postacıoğlu[7], Uğur Dogan[8], Hayrullah Karabulut[9],

7 Gülsen Uçarkuş[3], M Namık Çağatay[3]

9 [1]Aix Marseille Univ, CNRS, IRD, INRAE, Coll France, CEREGE, Aix-en-Provence,

10 France, [2]Istanbul Technical University, Eurasia Institute of Earth Sciences, Maslak,

11 Istanbul, Turkey, [3]Istanbul Technical University, Geological Engineering Dept.,

12 Maslak, Istanbul, Turkey, [4]CNRS, DT INSU, Parc national d'instrumentation

13 océanographique, Plouzané, France, [5]Aanderaa Data Instruments AS, Bergen,

14 Norway, [6]Aix Marseille Univ, CNRS, IRD, MIO, Aix-en-Provence, France, [7]Istanbul

15 Technical University, Physics Dept., Maslak, Istanbul, Turkey, [8]Yıldız Technical

16 University, Geomatic Engineering Dept., Istanbul, Turkey, [9]Bogazici University,

17 KOERI, Istanbul, Turkey

19 *Correspondence to*: Pierre Henry (henry@cerege.fr)

21 **Abstract.** Earthquake-induced submarine slope destabilization is known to cause

22 debris flows and turbidity currents, but the hydrodynamic processes associated with

23 these events remain poorly understood. Records are scarce and this notably limits

24 our ability to interpret marine paleoseismological sedimentary records. An

25 instrumented frame comprising a pressure recorder and a Doppler recording current

26 meter deployed at the seafloor in the Sea of Marmara Central Basin recorded

27 consequences of a $M_W = 5.8$ earthquake occurring Sept 26, 2019 and of a $M_w = 4.7$

28 foreshock two days before. The smaller event caused sediment resuspension but no

29 strong current. The larger event triggered a complex response involving a mud flow

30 and turbidity currents with variable velocities and orientations, which may result from

31 multiple slope failures. A long delay of 10 hours is observed between the earthquake

32 and the passing of the strongest turbidity current. The distance travelled by the

33 sediment particles during the event is estimated to several kilometres, which could

34   account for a local deposit on a sediment fan at the outlet of a canyon, but not for the

35   covering of the whole basin floor. We show that after a moderate earthquake,

36   delayed turbidity current initiation may occur, possibly by ignition of a cloud of

37   resuspended sediment. Some caution is thus required when tying seismoturbidites

38   with earthquakes of historical importance. However, the horizontal extent of the

39   deposits should remain indicative of the size of the earthquake.

40   1. Introduction

41   Triggering of mass flows and turbidity currents by earthquakes is a hazard that

42   can damage infrastructure at the seafloor (Heezen et al., 1954) and may enhance co-

43   seismic tsunami generation (Okal and Synolakis, 2001; Synolakis et al., 2002; Hebert

44   et al., 2005; Ozeren et al., 2010). It is often considered that a peak ground acceleration

45   (PGA) of the order of 0.1 g is needed for an earthquake to trigger a submarine slope

46   instability (Dan et al., 2008; Nakajima and Kanai, 2000). However, a global compilation

47   of cable breaks shows that, exceptionally, mass flow have been triggered by individual

48   earthquakes of M_w as low as 3.1 (with PGA $\approx 10^{-3}$ g) and that, on the other hand many

49    $M_w > 7$ have failed to break cables, notably in zones (e.g. Japan Trench) where

50   sediment input is relatively low and earthquakes frequent (Pope et al., 2016). In the

51   Mediterranean region, the threshold is reportedly around $M_w = 5$.

52   In spite of this high regional variability, turbidite deposits in several seismically

53   active zones have been used successfully as paleoseimological event markers

54   (Goldfinger et al., 2003, 2012; McHugh et al., 2014; Ikehara et al., 2016). This requires

55   distinguishing between seismoturbidites, caused by earthquakes and related mass

56   wasting events, from those resulting from other processes (e.g. floods, storms,

57   sediment loading). Seismoturbidites are generally described as turbidite-homogenites

58   where a basal silt-sand bearing layer is overlaid by a layer of apparently homogenous

59   mud with small or gradual, if any, variations in grain size and chemical composition

60   (Polonia et al., 2013; McHugh et al., 2011; Çağatay et al. 2012; Eriş et al., 2012;

61   Gutierrez-Pastor et al., 2013; Beck et al., 2007). In lakes and closed basins several

62   characteristics of deposits following earthquake or landslides, such as the sharp

63   boundary between turbidite and homogenite layers, the alternation of silt/sand and

64   mud laminae within a single turbidite-homogenite unit and presence of bi-directional

65   cross- or flaser- bedding have been interpreted as indicators of deposition from

66   oscillatory currents associated with seiches or turbidity current reflection (Beck et al.,

67   2007; Çağatay et al. 2012; McHugh et al., 2011). Seismoturbidites on ocean margins

68   have fairly similar characteristics to those in closed basins but their layering has been

69   interpreted differently, as a consequence of confluence (stacked or amalgamated

70   turbidites) or current speed variations (multi-pulsed turbidites) (Gutierrez-Pastor et al.,

71   2013; Nakajima and Kanai, 2000; Goldfinger et al., 2003). There is currently a lack of

72   in situ records that could substantiate inferred hydrodynamic processes. Monitoring

73   experiments brought records of representative cases of turbidity currents flowing in

74   submarine canyons and initiated by meteorological events and occasionally by

75   landslides (Azpiroz-Zabala et al., 2017; Khripounoff et al., 2012; Xu et al., 2004, 2010;

76   Liu et al., 2012; Hughes Clarke, 2016). Oscillatory currents resulting from internal

77   waves have been recorded after landslides in lakes (Brizuela et al., 2019). On the other

78   hand, most information on earthquake-triggered events is still indirect based on cable

79   ruptures (e.g. Pope, 2017; Hsu et al., 2008), combined with geomorphological and

80   sedimentological observations (Cattaneo et al., 2012; Piper et al., 1999), and

81   information from displaced instruments (Garfield et al., 1994). In Japan, in situ records

82   of pressure and temperature were obtained from displaced OBSs after the Tohoku

83   2011 M_w 9.1 earthquake (Arai et., 2013), and from cabled observatories after the

84   Tokachi-Oki 2003 M_w 8.3 earthquake (Mikada et al., 2006) and after a moderate (M

85   5.4) earthquake off Izu Penninsula (Kasaya et al., 2009). After the large events, strong

86   currents of more than 1 m/s were implied starting 2-3 hours after the earthquake with

87   no indication of oscillation or pulsing. In the off-Izu case a mudflow was observed with

88   a camera 5 minutes after the earthquake and followed 15 minutes later by a change in

89   current direction and speed.

90   We here present results from an instrumental deployment at the seafloor that

91   accidentally recorded the consequences of earthquakes that occurred 09/24/2019 and

92   09/26/2019 in the Sea of Marmara with respective magnitudes 4.7 and 5.8 (Figure 1A).

93   Holocene seismoturbidite records in the Sea of Marmara basins display a recurrence

94   of 200 to 300 years, that roughly corresponds to the recurrence interval of Mw>7

95   earthquakes (McHugh et al., 2006, 2014; Drab et al., 2012, 2015; Yakupoğlu et al.,

96   2018; Bulut et al., 2019). The pressure, temperature and current record from this single

97   instrument demonstrate that this moderate earthquake triggered turbidity currents.

98   However, the instrument suffered a rather complex sequence of disturbances and a

99   10 hours delay is observed between the earthquake and the recording of peak current.

100 We here propose a scenario which could explain the observations and discuss their

101 implications for the understanding of seismoturbidite records.

102
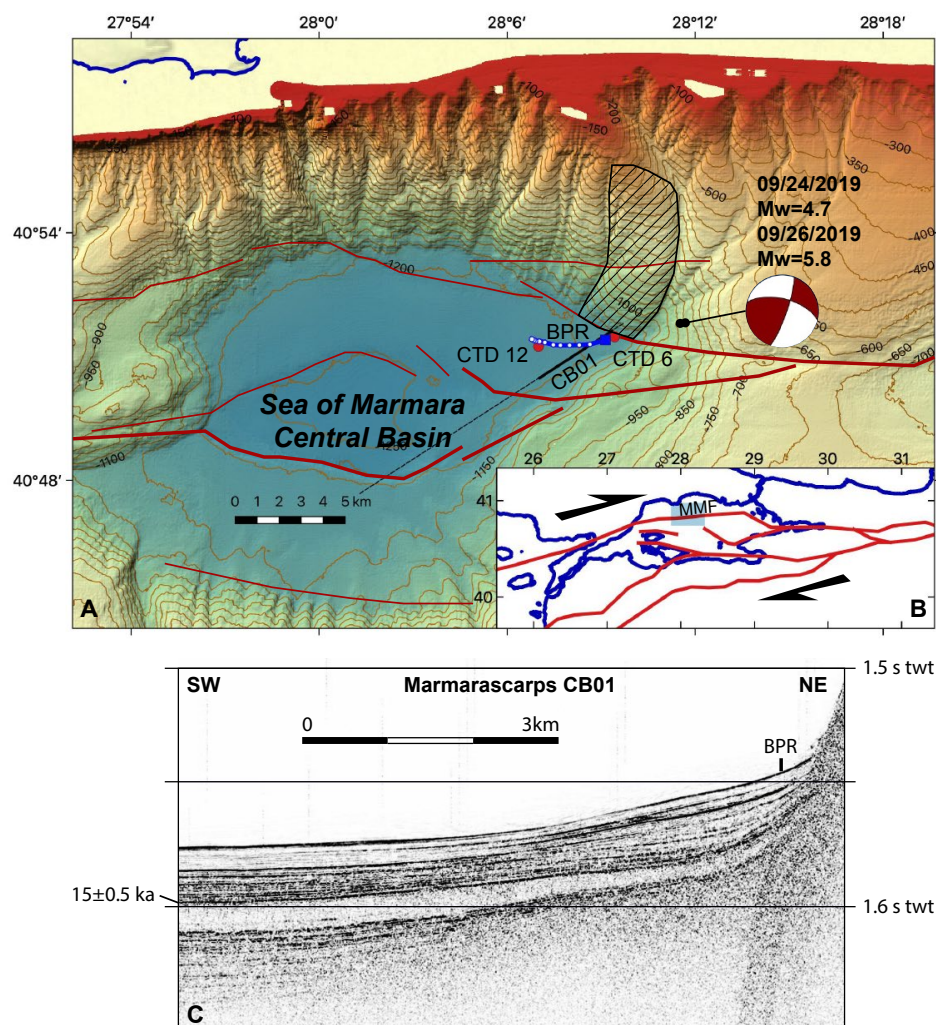
Figure 1. Context of instrumental deployment. (**A**) bathymetric map of the Sea of

104 Marmara Central Basin with simplified fault geometry (in red). The hatched zone is a

105 suspected mass wasting zone (Zitter et al., 2012). Location of instrumented frame

106 comprising bottom pressure recorder (BPR) and doppler current meter is indicated by

107 blue square. The blue banana with white dots represents the calculated trajectory of

108 a sedimentary particle during the waning phase of the turbidity current. Red dots are

109 CTD profiles 6 and 12 shown in supplementary material S1. Epicenter location of

110 earthquakes and the focal mechanism of the main shock are indicated. (**B**) Location

111 of study area. North Anatolian Fault system is shown in red. MMF is the Main

112 Marmara Fault. (**C**) Sediment sounder profile from Marmarascarps cruise (Armijo and

113 Malavieille, 2002). Indicative age of reflector from Beck et al. (2007). The instrument

114 (BPR) was deployed on a depositional fan at the base of slope and canyon outlet that

115 differ in character from the hemipelagite / turbidite-homogenite sequence in the

116 basin.

2. Context and data collection

118   A series of instrumental deployments was planned to record naturally occurring

119 resonant water column oscillations (seiches) at various locations in the Sea of

120 Marmara with the aim to improve tsunami models (Henry et al., 2021). An instrumented

121 frame was thus deployed at 40.8568° N, 28.1523° E and 1184 m water depth in the

122 Central Basin on May 9, 2019 and recovered 6 months later (11/19/2019) (Figure 1A).

123 This site is located at the outlet of a branched canyon system originating from the edge

124 of the continental shelf (Figure 1). Sediment sounder profiles indicate a depositional

125 fan or lobe is present at this location (Figure 1C). The short canyons observed on the

126 relatively steep sedimented slope (≈10°) of the Sea of Marmara deep basins are

127 presumably fed by instabilities of the canyon heads and walls (Zitter et al. 2012;

128 Çağatay et al., 2015). In addition, the slope west of the canyons immediately north of

129 the deployment site hosts a mass wasting feature covering about 24 km^2 (Zitter et al.

130 2012). The Main Marmara Fault (MMF, Figure 1B), is defined as the part of the northern

131 branch of the North Anatolian Fault system crossing the Sea of Marmara (Le Pichon

132 et al., 2001, 2003). A splay of the MMF runs along the base of this slope (Armijo et al.,

133 2002; Grall et al., 2012; Sengor et al., 2014). The 09/24/2019 and 09/26/2019

134 earthquakes occurred beneath the canyon system and their epicenters are located 5

135 km ENE of the instrument, less that 500 m apart (Figure 1). The rupture occurred within

136 the crust at 9-13 km depth on a northward dipping fault located north of principal

137 displacement zone of the Main Marmara Fault. The focal mechanism and aftershock

138 distribution indicate right-lateral strike-slip with a reverse component (Karabulut et al.,

139 2021). The rupture did not reach the seafloor, nor caused a tsunami. For instance, tidal

140 gauge records obtained at Marmara Ereglisi do not deviate more than 1hPa from a

141 fitted tidal model.

142   The instrumentation on the frame comprises (1) an RBR bottom pressure recorder
143   (BPR) with a Paroscientific 0-2000 m Digiquartz sensor, (2) a Seaguard recording
144   current meter (RCM) equipped with a Z-pulse 4520 Doppler current meter operating in
145   the 1.9-2 MHz frequency range and other sensors: temperature, pressure (tide sensor
146   Aanderaa 5217), conductivity (Aanderaa 4319), oxygen (Aanderaa optode 4330)
147   (Figure 2). The RBR pressure recording interval was set to 5s and that of the Seaguard
148   RCM to one hour for all sensors. The Doppler current meter worked in burst mode,
149   averaging 150 pings taken every second at the end of each one-hour recording interval.
150   The SeaGuard instrument was fixed on the upper part of the frame 1.5 m above the
151   seafloor and emit 4 narrow (2°) beams at orthogonal directions in a plane, parallel to
152   the seafloor if the frame is standing upright, and measures Doppler backscatter in cells
153   extending 0.5-to-2 meters from the instrument (Figure 3). The instrument was set in
154   forward ping mode, so that only data from sensors measuring a positive Doppler shift,
155   upstream currents moving toward the instrument, are used to calculate current speed.
156   The tide sensor is a piezoresistive sensor with a specified accuracy comparable to that
157   of the Digiquartz sensors (4kPa for a 0-2000 m sensor vs. 2kPa for a Digiquartz sensor
158   with the same range) and 0.2 hPa (2 mm) resolution and comprises a temperature
159   sensor of 0.2°C accuracy and 0.001°C resolution. The tide sensor averages pressure
160   measured at a 2 Hz sampling rate over 300 s at the end of each one-hour time interval.
161   the tide sensor was checked against an atmospheric reference between deployments
162   and found to have a minimal drift, less than 1 hPa.
163   As we will show that the 09/24/2019 earthquake caused the instrumented device
164   to lay on its side for several hours and then straighten up, understanding the setup of
165   the seafloor device and its stability is important (Figure 2B). The frame is made of
166   aluminium and has 6 rigidly bound flotation spheres of 25 kg buoyancy each. The net
167   weight of the instrumented frame in water is -80 kg. The frame is rigidly attached to a
168   12-cm-thick 1.5x1.3 m concrete slab, weighting 300 kg in water. The assembly of the
169   heavy slab and buoyant frame is stable in upright position in the water and on the
170   seafloor. Moreover, it is estimated that a current of 1 m/s would cause a total horizontal
171   drag of 75 kg when the device is in upright position, which is insufficient to destabilize
172   it. If a stronger current, or other external forces, cause the assembly to tilt and lay on
173   one side, the moment of the gravity and buoyancy forces should straighten the device
174   back to upright position when these external forces are removed.

175 Measurement of current speed and direction by a tilted instrument is a related issue
176 that we here consider. The orientation and attitude of the Seaguard RCM is measured
177 with a 2-component accelerometer and a magnetic compass and the recorded data
178 include tilt in X and Y direction and the heading of the X axis. Tilt X and Y components
179 are factory calibrated from -35° to +35° with an accuracy of 1.5°. Tests performed in
180 the laboratory (see supplementary material, Figure S1) showed that tilt information
181 remains consistent outside this range, even when the instrument is upside down. Tilt
182 measurements are accurate within 3° up to 60° but saturate at about 80° (Figure S2).
183 Uncertainty on heading also increases with tilt, especially when the instrument is tilted
184 toward the X-direction. However, measured heading remains ±20° of true heading for
185 a tilting of up to 60° (Figure S3). The current measured in the instrument plane is
186 corrected for tilt assuming current is horizontal. As far as this approximation is valid,
187 the current record should in principle remain fairly accurate when the instrument is
188 tilted beyond the normal range of operation (±35° degree) and at least to 60°. However,
189 the compass was not calibrated for an upside-down configuration. If the top of the
190 instrument would happen to be oriented downward, the measured current direction will
191 be unreliable, even though the absolute speed may still be correctly estimated. Another
192 problem may arise if one of the Doppler sensors is facing down into the sediment so
193 that its measurement cell is below the seafloor. If the sensor pointing upward in the
194 opposite direction is recording a negative Doppler shift, this value will be ignored in the
195 forward ping mode. In this case, the measurement retained to calculate current velocity
196 will correspond to noise from the sensor facing toward the seafloor. In all situations, it
197 remains possible to recalculate the sensor readings retained by the calculator from the
198 current velocity and orientation parameters recorded by the instrument, and thus
199 assess the reliability of data.
200

201
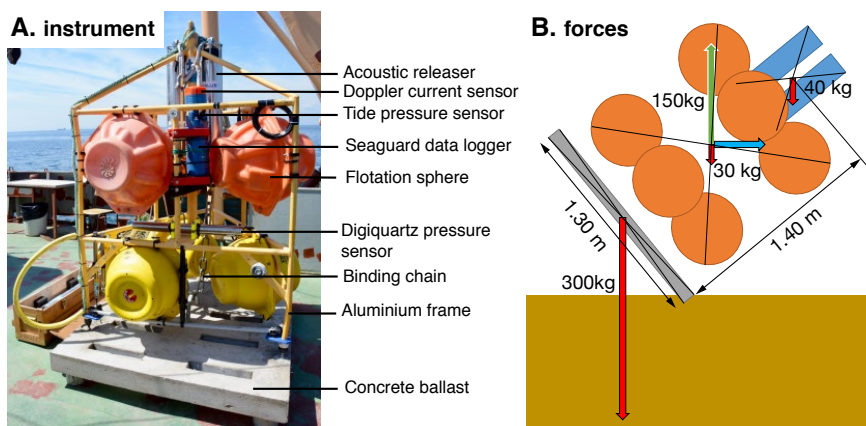
Figure 2. Instrumented frame. (A) photo of the instrumented frame before
deployment. (B) Sketch showing forces applied to the elements of the instrumented
frame in water. The red arrows represent the weight in water of the cement ballast, of
the instrumented frame and of the acoustic release system on top. The green arrow
represents the buoyancy of the flotation spheres. The blue arrow represents the
current drag, which depends on current speed and instrument tilt.

208

209

210
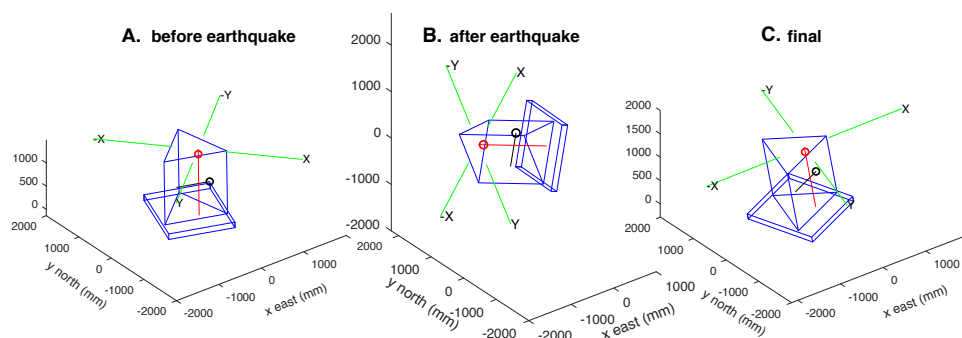
Figure 3. Reconstruction of frame position based on instrument tilt-meter and
compass data: (A) before the earthquake; (B) Tilted, between, 25 minutes and 10.5
hours after earthquake; (C) back in nearly upright position 11 hours after earthquake.
Position of Digiquartz pressure sensor (black circle), Aanderaa tide sensor (red
circle) and Doppler current meter beam cells (green segments)

216

217

3. Results and interpretations

3.1. Pressure and tilt records

Pressure sensors are sensitive to pressure variations caused by P-waves and Digiquartz sensors are also intrinsically sensitive to acceleration, but to a small extent, 160 hPa/g for an instrument with 20 MPa range according to the calibration report. Small earthquakes are detected as pressure spikes, while oscillations are recorded after large earthquakes. The M_w 4.7 09/24/2019 caused a short pressure transient of 25 hPa at 08:00:26 followed by small pressure oscillations of less than 3 hPa amplitude decaying over a few minutes. The seismic wave train from the M_w 5.8, 09/26/1919 earthquake is recorded by the Digiquartz pressure sensor as oscillations, initiated by a pressure drop of 65 hPa between 10:59:22 and 10:59:26 (Figure 4). For the sampling interval of 5s used in this setup, the recorded signal is aliased, which precludes quantitative interpretation in term of velocity or acceleration. However, the initial pressure drop after the 09/26/1919 earthquake may indicate a negative polarity of the first P arrival at the instrument site, located on an ascending ray-path.

Twenty-five minutes after the M_w 5.8, earthquake, a new disturbance of the pressure sensor is observed at 11:23:41. The pressure then progressively increases by 30.9 hPa in 15 seconds between 11:24:46 and 11:25:01 before stabilizing. Over the corresponding one-hour-time-interval between successive records, the Seaguard RCM, initially subvertical (tilt less than 2°), acquires a strong tilt (Figure 3). At 11:57:48, measured tilt is -65° along the X-axis and +19° along the Y-axis, with X-axis in a N161° azimuth and these values remain constant ±2° over the next 10 hours, corresponding to an absolute tilt of 68° (Figure 4). The tilting of the instrument causes the Digiquartz and Tide sensors to record different pressure variations because they are located at different positions on the frame (Figure 2). Moreover, the pressure readings by the Digiquartz sensor also depend on its orientation relative to Earth gravity. Pressure at the Tide sensor location increases about 100 kPa, corresponding to a 1 m drop and indicating that the frame was then practically laying on its side. Ten hours later, the device apparently straightens itself in about 5 seconds, between 21:28:29 and 21:28:34 as indicated by a rapid pressure variation. After that, the recorded tilt parameters are moderate and stabilize at -11.5° for the X-axis and 5.3° for the Y-axis, with X-axis in a N105.3° azimuth.

250   The M_w 4.7 earthquake caused minor disturbances of the attitude of the

251   instrument, with variations of tilt and heading of less than 0.5°. A M_w 3.6 foreshock of

252   the M_w 5.8 occuring 26/09/2019 at 7:32 also caused minor disturbances. These

253   indicate that the seafloor was sensitive to ground shaking caused by these small

254   earthquakes, however, this did not cause the device to sink into the sediment. Changes

255   of pressure baseline of the digiquartz sensor between before and after these

256   earthquake are difficult to resolve, and correspond to less than 5 mm vertical

257   displacement for the first event and less than 2 mm for the second one.

258
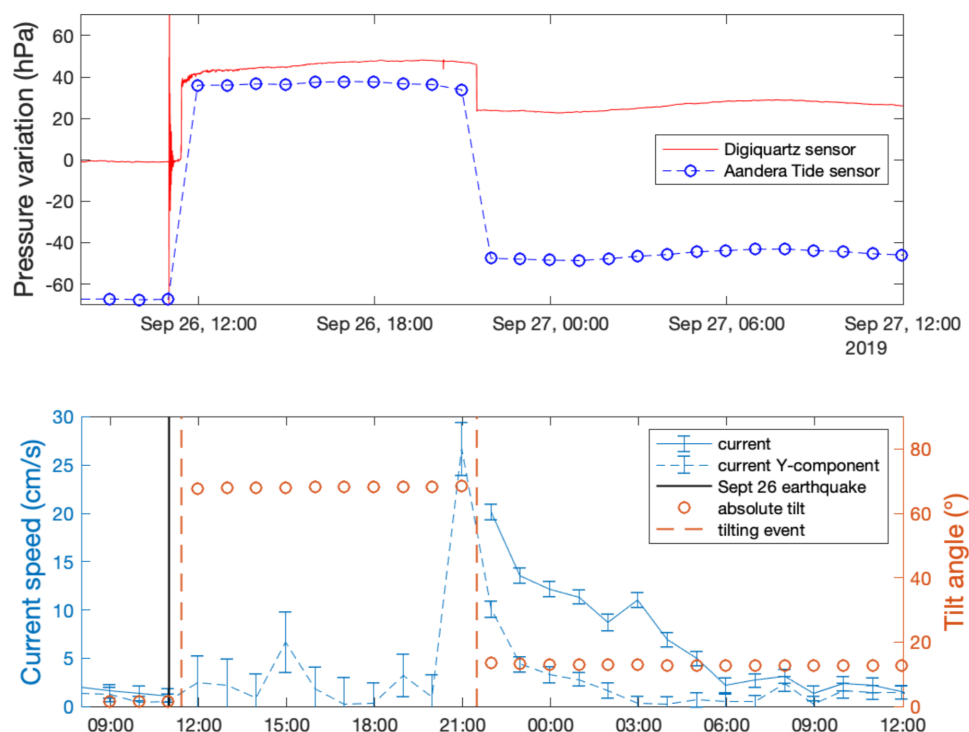
259

260   **Figure 4.** Time series around the time of occurrence of a M_w 5.8 earthquake; (top)

261   pressure variations recorded by two instruments on the instrumented frame; (bottom)

262   current and tilt data recorded by Seaguard RCM. Between the tilting events only one

263   component of the doppler current meter functioned reliably (Y-component oriented

264   N200) and is here reported.
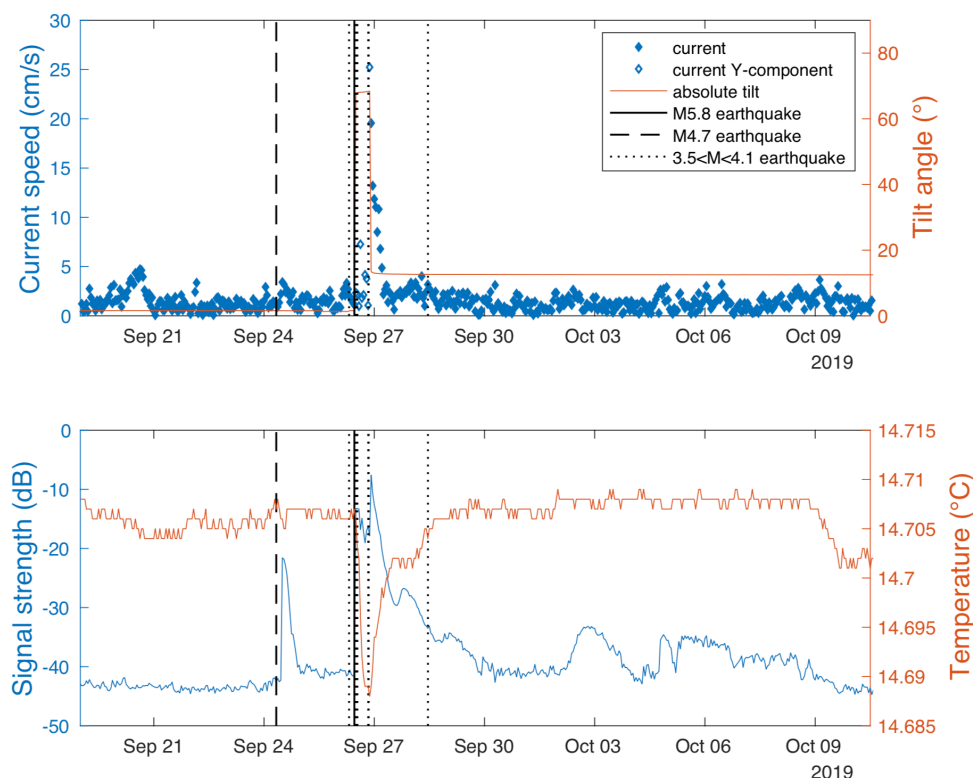
Figure 5. Time series acquired with Seaguard RCM during the September 2019 seismicity cluster; (top) current speed and tilt; (bottom) backscatter signal strength and temperature.

3.2. Current records and possible causes of tilting

The M$_w$ 4.7 09/24/2019 earthquake was followed by a small increase of current strength peaking at 3.4 cm/s at noon, 4 hours after the earthquake (Figure 5). Comparable events in term of duration and strength occurred spontaneously 09/20/2019 (with currents up to 4.7 cm/s) and 09/26/2019 just before the main earthquake. During all three events the dominant current was from the east, thus coming from the direction of the canyon, but there is an important difference between the event that occurred after the earthquake and the two others. During that event a change in current direction occurred from eastward to westward between 10:57 and 11:57 while the current strength increased from 2.2 cm/s to its peak value (Figure 6). During the other events, build-up was more progressive and did not involve a change in direction. A drift plot, calculated by summing velocity vectors over time, reproduces

282   the motion of a particle assuming a uniform velocity field (Figure 6). The total drift is

283   about 500 m and occurs in the 8 hours following the current inversion. Current direction

284   varies from Westward to Northward during this time interval.

285

286

287
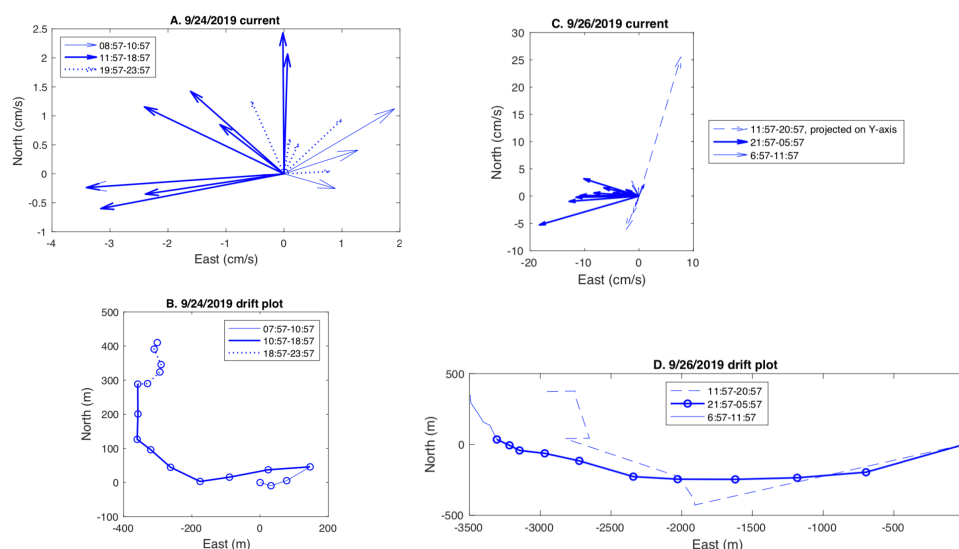
288   **Figure 6.** Current recorded after M_w 4.7 and M_w 5.8 earthquakes: (A) Current velocity

289   arrows recorded every hour between 08:57 and 23:57 on 09/24/2019; (B) drift plot

290   over the same time interval, the change of current direction and strength between

291   10:57 and 11:57 coincides with increasing backscatter strength (see figure 4),

292   indicative of increased turbidity; (C) Current velocity arrows recorded every hour

293   between 12:00 09/26/2019 and 06:00 09/27/2019. Dashed arrows show

294   measurements acquired in the Y direction when the instrument was strongly tilted

295   (position B in Figure 3), plain arrows when it was back in upright position (C in Figure

296   3); (D) drift plot over the same time interval, the dashed part corresponds to the

297   strongly tilted position.

298

299   After the M_w 5.8 09/26/1919 earthquake, during the 10 hours period when the

300   instrument remained strongly tilted, the instrument recorded currents varying both in

301   speed and orientation, but some precautions are needed when interpreting these data.

302   The current component measured by transducers along the Y-axis of the instrument,

303   oriented N200°, probably remained accurate as the tilt along this axis is less than 20°

304 and the measurement cell remained above the bottom (Figure 2B). On the other hand,

305 the X-component may not be reliable as one of the sensors (n°1) is oriented 65°

306 upward in the N160° direction, and the oposite sensor (n°3) is dipping 65° downward

307 in the opposite (N340°) direction. Consequently, measurement cell n°3 lies within the

308 sediment and thus may only record noise. Moreover, because the Doppler current

309 sensor (DCS) is set in forward pinging mode, current speed is calculated with data

310 from sensors measuring positive doppler shifts only. This implies that if the current

311 component toward N160° is positive, sensor n°1 will measure a negative shift and will

312 not be recorded. During the time inteval here considered, the mesured current

313 component in the X-direction (toward N160) is positive, which indicates that data from

314 sensor n°4 was used (Figure 7), and that is probably noise. It follows that the current

315 component along the Y-direction is the only one reliable. The horizontal current

316 measured along the Y-axis changed sign several times during this time interval, and

317 reached peak values of 6.3 cm/s toward N200 at 14:57:46, about four hours after the

318 earthquake, and of 25 cm/s in the oposite direction at 20:57:46, the last measurement

319 before the instrument straightenned up. Other measurements on both axes remain

320 below 5 cm /s, but the absolute velocity may have been higher because this

321 measurement was only performed in one direction. Yet, these observartions suggest

322 that the strong current recorded before the instrument straightenned up played a role

323 in this event. Once the device got back in an upright position, it recorded a current

324 consistently flowing westward and progressively decreasing from 20 cm/s to

325 background level (2 cm/s) in 9 hours (Figure 4). During this waning phase, the current

326 drift is about 3.5 km in a westward direction (Figure 6). The drift estimated during the

327 first 10 hours after the earthquake, while the instrument was strongly tilted, is in the

328 opposite direction but may not be reliable.

329

330
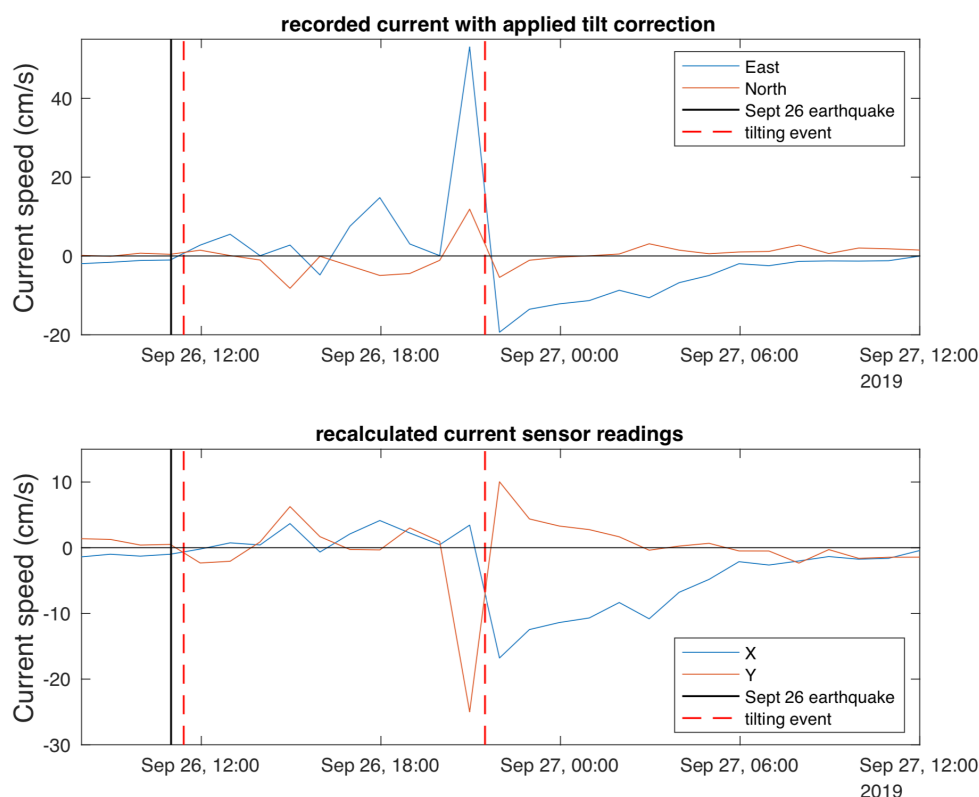
Figure 7. Current record acquired around the time of occurrence of a M_w 5.8
earthquake. A. Instrumental record, automatically corrected for tilt and heading. B.
recalculated readings in the X and Y axis of the Doppler sensor (see text for
interpretation).

335

  The current speed in the first 2 hours after the main earthquake apparently
remained low, at most 5-6 cm/s. It is thus unlikely that the tilt of the device was caused
by strong currents. Some short burst of current may have been missed because of the
1 hour sampling interval, but this would not explain why the frame then remained stable
in a tilted position for several hours. Local liquefaction of the sediment beneath the
device is also an unlikely cause because the tilting of the instrument occurred 25
minutes after the earthquake. A mud flow originating from the basin slopes thus
appears as a more likely cause. This hypothesis would also acount for the presence
of sandy mud caked on the device in various places: on the frame feet, on the acoustic
releasers, on the optode connector and also inside the plastic protection of a flotation

346   sphere, from which bindings were broken and had to be repaired. On the other hand,

347   the current speed in the 20-50 cm/s range recorded before, as well as after, the time

348   when the device straightened up is strong enough to cause erosion of mud or sand

349   deposits. It may thus be hypothesized that erosion freed the device from the mud cover.

350   The flotation spheres on the frame and the concrete ballast at its base exert a moment

351   that should keep the assembly stable in an upright position unless the frame is loaded

352   with sediment.

353

354   3.3.   Acoustic backscatter record

355   The strength of the backscattered signal can be used as a proxy for turbidity.

356   The Seaguard RCM emits in the 1.9-2 MHz band corresponding to a wavelength (λ) of

357   750 μm. Doppler backscatter current meters have maximum sensitivity for particles of

358   diameter $D = λ/π$ and can detect particles down to diameter $D = 0.08 λ$, for which

359   backscatter power is less than 1/10 of peak backscatter power (Guerrero et al., 2011,

360   2012). The seaguard RCM should thus be mostly sensitive to the presence in

361   suspension of sand size particles (larger than 63 μm). The background backscatter

362   amplitude level is -43±1dB before the earthquakes. Three to four hours after the M_w

363   4.7 09/24/2019 earthquake, backscatter increases sharply to -22dB between 11:00

364   and 12:00, and then decays to -41dB in 12 hours. The increase of backscatter

365   coincides with a change of current direction and speed, indicating that the turbid cloud

366   was brought to the instrument site by the current. However, the current speed of less

367   than 4 cm/s may have been insufficient to put the particles in suspension. There is no

368   increase of backscatter on Sept 20 when stronger currents coming from the same

369   direction, but not related with an earthquake, were recorded.

370   Backscatter strengh remain 41±1 dB the 1.5 days interval before the M_w 5.8

371   09/26/1919 and increases to the -20 dB to -13 dB range after the earthquake (Figure

372   5), which implies sand sized sediment was put in suspension soon after the earthquake

373   although the local current speed remained relatively low (about 5 cm/s at most). After

374   the device went back to near vertical position, signal strengh reaches a maximum of -

375   7.6 dB, which correspond to an amplitude ratio of 42 and an intensity ratio of 1800

376   compared to base level. Similar signal strength levels are typically reached with the Z-

377   Pulse sensor in highly turbid water such as in estuaries. During deep sea deployments

378   signal strength range more typically between -60 and -40 dB. After reaching peak value,

379   backscattered signal strength progressively decays to stabilise at about -40 dB 3 days

380   (Figure 5). Several turbid events, with signal strength about -35 dB are observed in

381   October and associated with small increases in current velocity (up to 3-4 cm/s). It is

382   unclear whether these passing clouds are residual turbidity from the earthquake. After

383   October 9, backscatter eventually returns to background level while temperature

384   decreases by 0.007 °C over a few hours, indicating replacement of the water mass

385   around the instrument.

386

387   3.4. Temperature record

388   The Sea of Marmara is stratified, with a low salinity (20-22‰) 20-30 m surface

389   layer that displays strong seasonal temperature variability overlaying a high salinity

390   (about 38‰) body of seawater at 14-15°C derived from the Aegean Sea (Beşiktepe et

391   al., 1994). Within this body, the potential temperature generally decreases with depth,

392   which would in principle imply that a turbidity current, flowing downward, should cause

393   a small temperature increase. However, the deployment site is prone to seasonal

394   cascading, so that the initial temperature structure may have been disturbed. Example

395   of CTD profiles recorded in June 2007 (Henry et al., 2007) are shown in Figure 8. No

396   CTD profile is available in Sept 2019, but variations in temperature and oxygen

397   concentration associated with mild currents (<5 cm/s) were recorded by the instrument

398   in May-July 2019, and again on Sept 20.

399   Temperature variations associated with the M_w 4.7 09/24/2019 earthquakes are

400   very small, less than ±0.002°C, which confirms that water did not travel far during this

401   event. After the M_w 5.8 09/26/1919 earthquake, the recorded temperature decreases

402   progressively by about 0.015°C, after the first hydrologic disturbance and tilting of the

403   instrument, until the recorded current reaches its maximum value (Figure 5).

404   Temperature then progressively increases to reach nearly the same value as before

405   the event. The small variation in temperature recorded indicates that the turbid water

406   originates from the deep-water body. The slight temperature decrease observed after

407   the earthquake can result from the mixing of a warmer bottom water layer with the bulk

408   of the deep-water layer. However, the observation of a temperature drop precludes

409   that the turbid water originates from depths less than 400 m, as water present between

410   400 m and the halocline is at a higher potential temperature than the deeper water

411   throughout the year (see Beşiktepe et al., 1994, and figure 8). Moreover, an inflow of

412   water from closer to the surface should result in an increase in the O_2 concentration in

413   the bottom water, but none is observed in the data.

414
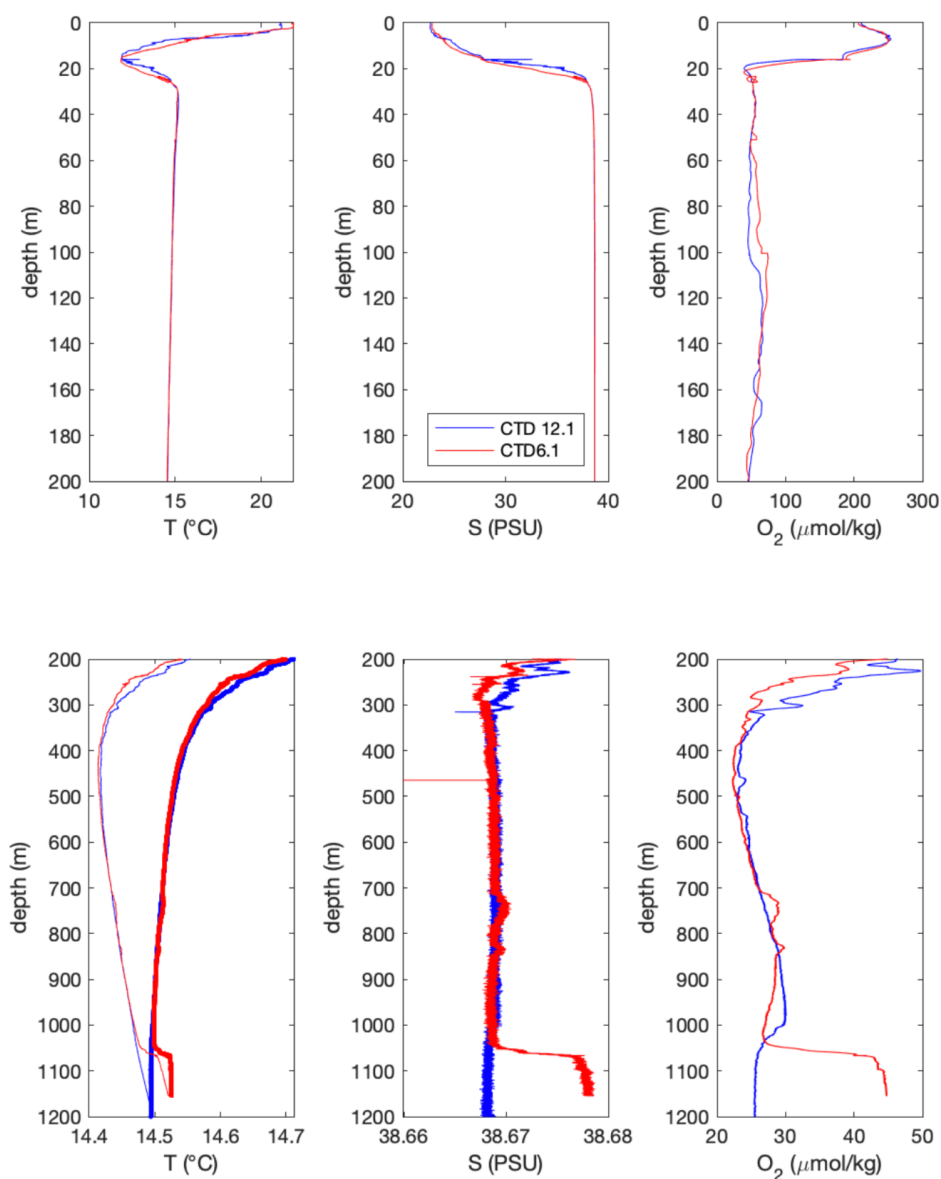
415

416   **Figure 8.** Depth plots of Temperature (°C), Salinity (PSU) and oxygen concentration

417   (µmol/kg) from CTD profiles acquired in the Sea of Marmara during Marnaut cruise of

418   Ifremer RV L'Atalante (Henry et al., 2007). On the lower temperature plot, thin lines

419 are measured values and thick lines are potential temperatures calculated at 1180 m.

420 Locations are shown on Figure 1

421

422 ### 3.5. Inferred sequence of events

423 These observations provide some insight on the complex sequence of events

424 that followed the earthquake and suggest the following scenario. After the M_w 4.7

425 09/24/2019 a turbid cloud formed east of the instrument and drifted slowly. Considering

426 the maximum velocity of the current (less than 4 cm/s) and the 4-hours interval

427 between the earthquake and the passing of the turbid cloud over the instrument, the

428 front of turbid water should have formed ENE of the instrument at a maximum distance

429 of about 500 m, and this coincides with the base of the northern slope near the outlet

430 of the canyon. It is suspected that instability on the steeper slopes on the sides of the

431 canyon is the primary cause of sediment suspension. The clouds subsequently drifted

432 downslope over a total horizontal distance of at most 1 kilometers before dissipating,

433 adding the 500 m estimate above to the drift calculated after the passing of the front

434 over the instrument (Figure 6).

435 The M_w 5.8 09/26/1919 caused much stronger currents. After the passing of

436 the seismic wave, triggering of instability on slopes adjacent to the deployment site

437 caused mud flows that spread on the basin floor causing the tilting of the instrument

438 25 minutes after the earthquake, and bottom water turbidity. As the base of the nearest

439 slope is about 400 m north of the instrument, this would imply a minimum velocity of

440 20 cm/s for the mudflow to reach the device location in 25 minutes. During the following

441 10 hours, the current record is incomplete but indicates variations in strength and

442 direction. Widespread slope instabilities triggered by the earthquake may have resulted

443 in several turbidity currents recorded as succesive pulses. The role of seiches and

444 surface gravity waves in sediment resuspension can be ruled out as no tsunami was

445 recorded by near shore tidal gauges around the Sea of Marmara. The relationship

446 between gravity wave amplitude A and bottom current amplitude U in the shallow water

447 linear approximation is given by $U=(g/H)^{1/2}A$, where H is water column height. An

448 oscillatory current of 10 cm/s at 1200 m depth would thus correspond to a free surface

449 oscillation of 1 m (or 100 hPa) for a standing wave (seiche) as well as a progressive

450 wave (tsunami). This should have been easily detected in a sea where tidal amplitude

451 is about 10 cm (Alpar and Yüce, 1998). The influence of baroclinic internal waves on

452 the halocline at 20-30 m depth must also be ruled out as they cannot physically
453 produce currents of more than a few cm/s at 1200 m. However, It remains possible
454 that the interface at the top of the turbid cloud is affected by baroclinic waves. The
455 strongest current is recorded after 10 hours, which suggests that a turbidity current
456 initiated further upslope may have reached the site after a longer delay but may also
457 have gained more kinetic energy on its downhill path. This event, reaching a speed
458 exceeding 25 cm/s apparently caused enough erosion to free the device from the mud
459 accumulation. The current then stabilizes in a westward direction and decays
460 progressively over the next 9 hours, which suggests the tail of a turbidity current flowing
461 in the canyon E of the deployment site has been recorded. The hours-long delay
462 between the earthquake and the passing of the fastest current over the instrument may
463 hypothetically correspond to the time for the head of the turbidity current to travel from
464 its source to the location of the instrument. The length of the canyon valley between
465 the device location and the 400 m isobath, inferred to be the minimum depth of the
466 turbid water source, is about 13 km. In this scenario, the average velocity of the head
467 of the turbidity current would be 30-40 cm/s. Alternatively, a sequence of slope failures
468 may have lasted up to several hours after the earthquake. The distance travelled by
469 the turbidity current on the basin floor beyond the instrument may be estimated from
470 the calculated drift during the waing phase, and is found to be about 3.5 km (Figure 6).
471 When plotted over the bathymetric map the drift appears to stay within the depositional
472 fan at the outlet of the cayon, the extension of which is known from sediment sounder
473 profiles (Figure 1). These calculations are only a rough estimate of the distance
474 travelled by suspended particles as only the velocity at 1.5 m above the seafloor is
475 known. However, it appears unlikely that sediments spread all over the 15x20 km basin
476 floor as this would require velocities of the order of 1m/s, sustained over a wide area
477 for several hours.

478   The decay of the backscatter signal strength over the next 3 days may reflect
479 the settling of sand size particles put in suspension in the water column after this
480 sequence of events. For a first order assessment, Stokes settling velocity, an upper
481 bound valid in dilute suspensions (e.g. Guazelli and Morris, 2012) may be used. The
482 Stokes settling velocity of 63 µm quartz grains (density 2650 kg/m^3) in 13°C seawater
483 is 2.7 mm/s, allowing such grains to drop by 700 m in 3 days. However, if the particles
484 forming the cloud are mostly composed of clay agregates, which density may be
485 comprised between 1200 and 1700 kg/m^3, the settling velocity would be comprised

486   between 0.3 mm and 1 mm/s. In this case the height of the suspended particle cloud
487   could range between 70 and 250 m.

4.   Discussion and conclusion

489   Data obtained with a seafloor device located at the oultet of a canyon in the
490   Central Basin in the Sea of Marmara bring some insight on how earthquakes scale
491   with their hydrodynamic consequences. In September 2019, M_w 4.7 and 5.8
492   earthquakes occurred at a 5 km distance from the device as well as a series of smaller
493   foreshocks and aftershocks In this setting, earthquakes of magnitude less than 4 did
494   not cause noticeable water column turbidity nor currents. The M_w 4.7 earthquake
495   generated a turbid cloud on slopes a few hundred meters from the instrument and the
496   cloud took 3-4 hours to drift down to the instrument location and 10 more hours to
497   dissipate. As the current velocity remained small (less than 4 cm/s), it can be concluded
498   that this cloud did not evolve into a self-sustained turbidity current (Parker, 1982). The
499   M_w 5.8 earthquake initiated a turbidity current and the data obtained may be compared
500   with more complete records of turbidity currents obtained elsewhere with ADCP
501   deployments and/or water column mooring lines. The duration of the event in the Sea
502   of Marmara (about 10 hours) appear fairly typical and comparable with events recorded
503   in other locations regardless of the initiation mechanism, which comprise hyperpycnal
504   flows from river floods (Var and Gaoping canyons), storm waves and dredging (Gulf of
505   St Laurence and Monterey canyon), and slope instabilities triggered by an earthquake
506   (Tokachi-oki) or by other processes (Var canyon) (Normandeau et al., 2019;
507   Khripounoff et al., 2012; Xu et al., 2004; Liu et al., 2012; Mikada et al., 2006). Longer
508   duration events with very different hydrodynamic characteristics have been observed
509   in larger scale systems (e.g. Congo deep sea canyon, Azpiroz-Zabala et al., 2017). On
510   the other hand, events recorded closer to shore on the edge of the continental shelf or
511   on a delta front have much shorter durations (Xu et al., 2010; Hughes Clarke, 2016).
512   In events of comparable scale to the Sea of Marmara one, the velocity of the current
513   generally reaches its maximum several meters above the seafloor, so that the velocity
514   recorded by our instrument at 1.5 m from the seafloor is within the boundary layer, and
515   lower than either the maximum current velocity or the velocity of the head of the
516   turbidity current. A velocity of several tens of centimeter per second is representative
517   of the slower recorded examples, corresponding to mud rich flows associated with
518   hyperpycnal flows, to the smaller landslides (Khripounoff et al. 2012) or to the smaller

519   storm-related events (Normandeau et al., 2019). Turbidites following large
520   earthquakes or large slope instabilities have reached maximum velocities of 20 m/s
521   (Piper et al., 1999). Velocities of 2-7 m/s were reported for the turbidity current following
522   Tohoku earthquake (Arai et al., 2013) and 1.4 m/s in the Tokachi-Oki case (Mikada et
523   al., 2006). The downward current after the off-Izu Penninsula earthquake may be
524   constrained with a noisy ADCP record to a maximum of 10-15 cm/s in a 20-30 m layer
525   above the seafloor and lasted about one hour, peaking about 30 minutes after the
526   earthquake (Kasaya et al., 2009). This turbidity current thus appears less intense and
527   shorter in duration than the one recorded in the Sea of Marmara, but the triggering
528   earthquake was also smaller (M5.4 compared to M5.8) and more distant (10 km).
529   These observations suggest that a general scaling relationship could exist between
530   earthquake magnitudes and the strength and extent of the turbidity currents they
531   induce. Moreover, although the off-Izu event is shorter than the Sea of Marmara one,
532   they share an important characteristic in that the turbid cloud is observed to form when
533   a mud flow hits the observatory site and some time before current builds up in the
534   water column.

535   The 10 hours delay observed in the Sea of Marmara between the triggering
536   event and the peak of the turbidity current is long compared to the 2 hours delay
537   observed after Tohoku and Tokachi-oki earthquakes. We suggested earlier that the
538   long delay may simply result from a slower velocity of the turbidity current or from
539   delayed slope failure. Another possibility is delayed ignition, which may occur if the
540   turbidity current develops indirectly from the hydrodynamic instability of a turbid cloud
541   resulting from slope failures and/or ground shaking rather than by acceleration of a
542   dense mud flow (Parker, 1982; Mulder and Cochonnat, 1996; Piper and Normark,
543   2009).

544   The scenario we propose for the Sept 26, 2019 earthquake involving mud flows
545   from proximal sources followed by turbidity currents originating at larger distances
546   and the subsequent settling of sediment in suspension, could relate with the structure
547   of turbidite-homogenite. Progressive or pulsed build-up of turbidity current energy is
548   considered typical of hyperpycnal flows initiated by river floods (Mulder et al., 2003)
549   but reverse grading and pulsing is also observed in seismoturbidites (Gutierrez-Pastor
550   et al., 2013). In the Sea of Marmara, many of the laminated turbidites sampled in
551   Kumburgaz Basin formed from the amalgamation (below the homogenite layer) of at
552   least two flows, the first one being finer and less sorted (Yakupoğlu et al., 2019). The

553 coarsening observed in this context is often associated with an increase of the calcium

554 content indicative of a shallower source, rich in biogenic carbonate material. However,

555 in the case observed in the present study, remobilization of sediment should be limited

556 to the lower slope as the temperature of the displaced water precludes a source

557 shallower than 400 m water depth.

558   The geomorphological context of the deployment site south of a slope identified

559 as unstable from geomorphological criteria (Zitter et al., 2012), and on a depositional

560 fan at the outlet of a canyon is also consistent with the proposed scenario. We

561 estimated by integrating recorded current velocity that the current during this event

562 was not strong enough to spread the sediment over the entire Central Basin floor but

563 that the zone of deposition was probably comparable in size to the fan. It can be

564 inferred that the paleoseismological record from a core taken in the fan should contain

565 more events than one taken at the basin depocenter. A sediment sounder profile

566 (Figure 1) also shows that the character of the seismic reflectors differs in the basin

567 and in the fan and that establishing reliable correlations between them is not simple.

568 However, as hypothesized by previous studies (McHugh et al., 2014), turbidite-

569 homogenite deposits that can be correlated between cores taken at various locations

570 in the basin probably correspond to the larger events, which may be correlated with

571 historical earthquakes. Moreover, it is still unknown whether the Sept 26 event left a

572 trace on the seafloor morphology and in the sediment record. Performing new core

573 sampling and very high-resolution geophysical surveys in this area would thus have

574 important implications for the understanding of seismoturbidite records and for the

575 assessment of geohazards.

576

577 Acknowledgements

578 Financial support was provided by the bilateral ANR/TÜBITAK collaborative research

579 project MAREGAMI (ANR-16-CE03-0010-02 and Tübitak Project 116Y371) and by

580 CNRS-INSU through the European Multidisciplinary Sea Observatory (EMSO)

581 Research Infrastructure program. DT-INSU and Istanbul Technical University

582 hydrodynamic engineering department provided technical support for device design,

583 construction, and deployment. Bernard Mercier de Lépinay provided processed

584 sediment sounder profiles. We thank the crew and Captain of R/V Yunus (Istanbul

585 University) for their support during installation and recovery of the instruments.

586 Seafloor monitoring data are available through SEANOE (Henry et al., 2021) and

587 CTD profile data through SISMER Oceanographic Data portal (Henry et al., 2007).

588

589 References

590 Alpar, B., & Yüce, H. (1998). Sea-level variations and their interactions between the Black

591   Sea nd the Aegean Sea. Estuarine, Coastal and Shelf Science, 46, 609–619.

592 Arai, K., Naruse, H., Miura, R., Kawamura, K., Hino, R., Ito, Y., Inazu, D., Yokokawa, M.,

593   Izumi, N., Murayama, M., & Kasaya, T. (2013). Tsunami-generated turbidity current of

594   the 2011 Tohoku-Oki earthquake. Geology, 41(11), 1195–1198.

595   https://doi.org/10.1130/G34777.1

596 Armijo, R., Meyer, B., Navarro, S., King, G., & Barka, A. (2002). Asymmetric slip partitioning

597   in the Sea of Marmara pull-apart: a clue to propagation processes of the North Anatolian

598   Fault? Terra Nova, 14(2), 80–86. https://doi.org/10.1046/j.1365-3121.2002.00397.x

599 Armijo, R. and J. Malavieille (2002) MARMARASCARPS cruise, RV L'Atalante,

600   https://doi.org/10.17600/2010140

601 Azpiroz-Zabala, M., Cartigny, M. J. B., Talling, P. J., Parsons, D. R., Sumner, E. J., Clare, M.

602   A., Simmons, S. M., Cooper, C., & Pope, E. L. (2017). Newly recognized turbidity current

603   structure can explain prolonged flushing of submarine canyons. Science Advances,

604   3(10). https://doi.org/10.1126/sciadv.1700200

605 Beck, C., Mercier de Lépinay, B., Schneider, J. L., Cremer, M., Çağatay, N., Wendenbaum,

606   E., et al. (2007). Late Quaternary co-seismic sedimentation in the Sea of Marmara's

607   deep basins. Sedimentary Geology, 199, 65–89.

608   https://doi.org/10.1016/j.sedgeo.2005.12.031

609 Beşiktepe, Ş. T., Sur, H. İ., Özsoy, E., Latif, M. A., Oğuz, T., & Ünlüata, Ü. (1994). The

610   circulation and hydrography of the Marmara Sea. Progress in Oceanography, 34(4),

611   285–334. https://doi.org/10.1016/0079-6611(94)90018-3

612 Brizuela, N., Filonov, A., & Alford, M. H. (2019). Internal tsunami waves transport sediment

613   released by underwater landslides. Scientific Reports, 9(1), 10775.

614   https://doi.org/10.1038/s41598-019-47080-0

615 Bulut, F., Aktuğ, B., Yaltırak, C., Doğru, A., & Özener, H. (2019). Magnitudes of future large

616   earthquakes near Istanbul quantified from 1500 years of historical earthquakes, present-

617   day microseismicity and GPS slip rates. Tectonophysics, 764(July 2018), 77–87.

618   https://doi.org/10.1016/j.tecto.2019.05.005

619 Çağatay, M. N., Erel, L., Bellucci, L. G., Polonia, a., Gasperini, L., Eriş, K. K., Sancar, Ü.,

620   Biltekin, D., Uçarkuş, G., Ülgen, U. B., & Damci, E. (2012). Sedimentary earthquake

621 records in the İzmit Gulf, Sea of Marmara, Turkey. Sedimentary Geology, 282, 347–359.

622 https://doi.org/10.1016/j.sedgeo.2012.10.001

623 Çağatay, N. M., Ucarkus, G., Eris, K. K., Henry, P., Gasperini, L., & Polonia, A. (2015).

624 Submarine canyons of the Sea of Marmara. In F. Briand (Ed.), Submarine Canyon

625 Dynamics in the Mediterranean and Tributary Seas, CIESM Workshop Monograph n° 47

626 (pp. 123–135). CIESM Publisher, Monaco. https://doi.org/10.13140/RG.2.1.1692.8402

627 Cattaneo, A., Babonneau, N., Ratzov, G., Dan-Unterseh, G., Yelles, K., Bracane, R., Mercier

628 De Lapinay, B., Boudiaf, A., & Daverchare, J. (2012). Searching for the seafloor

629 signature of the 21 May 2003 Boumerdas earthquake offshore central Algeria. Natural

630 Hazards and Earth System Science, 12(7), 2159–2172. https://doi.org/10.5194/nhess-

631 12-2159-2012

632 Dan, G., Sultan, N., Savoye, B., Deverchere, J., & Yelles, K. (2009). Quantifying the role of

633 sandy-silty sediments in generating slope failures during earthquakes: Example from the

634 Algerian margin. International Journal of Earth Sciences, 98(4), 769–789.

635 https://doi.org/10.1007/s00531-008-0373-5

636 Drab, L., Hubert Ferrari, A., Schmidt, S., & Martinez, P. (2012). The earthquake sedimentary

637 record in the western part of the Sea of Marmara, Turkey. Natural Hazards and Earth

638 System Science, 12(4), 1235–1254. https://doi.org/10.5194/nhess-12-1235-2012

639 Drab, L., Hubert-Ferrari, A., Schmidt, S., Martinez, P., Carlut, J., & El Ouahabi, M. (2015).

640 Submarine Earthquake History of the Çınarcık Segment of the North Anatolian Fault in

641 the Marmara Sea, Turkey. Bulletin of the Seismological Society of America, 105(2A),

642 622–645. https://doi.org/10.1785/0120130083

643 Eriş, K. K., Çağatay, N., Beck, C., Mercier de Lepinay, B., & Corina, C. (2012). Late-

644 Pleistocene to Holocene sedimentary fills of the Çinarcik Basin of the Sea of Marmara.

645 Sedimentary Geology, 281, 151–165. https://doi.org/10.1016/j.sedgeo.2012.09.001

646 Garfield, N., Rago, T. A., Schnebele, K. J., & Collins, C. A. (1994). Evidence of a turbidity

647 current in Monterey Submarine Canyon associated with the 1989 Loma Prieta

648 earthquake. Continental Shelf Research, 14(6), 673–686. https://doi.org/10.1016/0278-

649 4343(94)90112-0

650 Goldfinger, C., Nelson, C. H., & Johnson, J. E. (2003). Holocene earthquake records from

651 the cascadia subduction zone and northern san andreas fault based on precise dating of

652 offshore turbidites. Annual Review of Earth and Planetary Sciences, 31(1), 555–577.

653 https://doi.org/10.1146/annurev.earth.31.100901.141246

654 Goldfinger, C., Nelson, C. H., Morey, A. E., Johnson, J. E., Patton, J., Karabanov, E.,

655 Gutiérrez-Pastor, J., Eriksson, A. T., Gràcia, E., Dunhill, G., Enkin, R. J., Dallimore, A., &

656 Vallier, T. (2012). Earthquake Hazards of the Pacific Northwest Coastal and Marine

657 Regions Turbidite Event History — Methods and Implications for Holocene

658   Paleoseismicity of the Cascadia Subduction Zone Professional Paper 1661 – F. USGS,

659   Professional Paper 1661-F, 170. Retrieved from http://pubs.usgs.gov/pppp1661f/

660 Grall, C., Henry, P., Tezcan, D., Mercier de Lepinay, B., Becel, A., Geli, L., Rudkiewicz, J.-L.,

661   Zitter, T., & Harmegnies, F. (2012). Heat flow in the Sea of Marmara Central Basin:

662   Possible implications for the tectonic evolution of the North Anatolian fault. Geology,

663   40(1), 3–6. https://doi.org/10.1130/G32192.1

664 Guazzelli, E., Morris, J. F., & Pic, S. (2011). A Physical Introduction to Suspension

665   Dynamics. Cambridge: Cambridge University Press.

666   https://doi.org/10.1017/CBO9780511894671

667 Guerrero, M., Rüther, N., & Szupiany, R. N. (2012). Laboratory validation of acoustic Doppler

668   current profiler (ADCP) techniques for suspended sediment investigations. Flow

669   Measurement and Instrumentation, 23(1), 40–48.

670   https://doi.org/10.1016/j.flowmeasinst.2011.10.003

671 Guerrero, M., Szupiany, R. N., & Amsler, M. (2011). Comparison of acoustic backscattering

672   techniques for suspended sediments investigation. Flow Measurement and

673   Instrumentation, 22(5), 392–401. https://doi.org/10.1016/j.flowmeasinst.2011.06.003

674 Gutiérrez-Pastor, J., Nelson, C. H., Goldfinger, C., & Escutia, C. (2013). Sedimentology of

675   seismo-turbidites off the Cascadia and northern California active tectonic continental

676   margins, northwest Pacific Ocean. Marine Geology, 336, 99–119.

677   https://doi.org/10.1016/j.margeo.2012.11.010

678 Hébert, H., Schindelé, F., Altinok, Y., Alpar, B., & Gazioglu, C. (2005). Tsunami hazard in the

679   Marmara Sea (Turkey): A numerical approach to discuss active faulting and impact on

680   the Istanbul coastal areas. Marine Geology, 215, 23–43.

681   https://doi.org/10.1016/j.margeo.2004.11.006

682 Heezen, B. C., Ericson, D. B., & Ewing, M. (1954). Further evidence for a turbidity current

683   following the 1929 Grand banks earthquake. Deep Sea Research (1953), 1(4), 193–202.

684   https://doi.org/10.1016/0146-6313(54)90001-5

685 Henry, P., A.M.C. Şengör, M.N. Çağatay (2007) MARNAUT cruise, RV L'Atalante,

686   https://doi.org/10.17600/7010070

687 Henry, P., Özeren M.S., Desprez De Gesincourt O., de Saint-Leger E., Libes,, M., Çakir, Z.,

688   Yakupoğlu, N., Géli, L. (2021). EMSO / MAREGAMI Marmara bottom pressure and

689   current records. SEANOE. https://doi.org/10.17882/78928

690 Hsu, S. K., Kuo, J., Lo, C. L., Tsai, C. H., Doo, W. Bin, Ku, C. Y., & Sibuet, J. C. (2008).

691   Turbidity currents, submarine landslides and the 2006 Pingtung earthquake off SW

692   Taiwan. Terrestrial, Atmospheric and Oceanic Sciences, 19(6), 767–772.

693   https://doi.org/10.3319/TAO.2008.19.6.767(PT)

694 Hughes Clarke, J. E. (2016). First wide-angle view of channelized turbidity currents links
695   migrating cyclic steps to flow characteristics. Nature Communications, 7(1), 11896.
696   https://doi.org/10.1038/ncomms11896
697 Ikehara, K., Kanamatsu, T., Nagahashi, Y., Strasser, M., Fink, H., Usami, K., et al. (2016).
698   Documenting large earthquakes similar to the 2011 Tohoku-oki earthquake from
699   sediments deposited in the Japan Trench over the past 1500 years. Earth and Planetary
700   Science Letters, 445, 48–56. doi:10.1016/j.epsl.2016.04.009
701 Karabulut, H., Güvercin, S. E., Eskikoÿ, F., Konca, A. Ö., & Ergintav, S. (2021). The
702   moderate size 2019 September Mw5.8 Silivri earthquake unveils the complexity of the
703   Main Marmara Fault shear zone. Geophysical Journal International, 224(1), 377–388.
704   https://doi.org/10.1093/gji/ggaa469
705 Kasaya, T., Mitsuzawa, K., Goto, T., Iwase, R., Sayanagi, K., Araki, E., Asakawa, K., Mikada,
706   H., Watanabe, T., Takahashi, I., & Nagao, T. (2009). Trial of Multidisciplinary
707   Observation at an Expandable Sub-Marine Cabled Station "Off-Hatsushima Island
708   Observatory" in Sagami Bay, Japan. Sensors, 9(11), 9241–9254.
709   https://doi.org/10.3390/s91109241
710 Khripounoff, A., Crassous, P., Lo Bue, N., Dennielou, B., & Silva Jacinto, R. (2012). Different
711   types of sediment gravity flows detected in the Var submarine canyon (northwestern
712   Mediterranean Sea). Progress in Oceanography, 106, 138–153.
713   https://doi.org/10.1016/j.pocean.2012.09.001
714 Le Pichon, X., Chamot-Roooke, N., Rangin, C., & Sengör, A. M. C. (2003). The North
715   Anatolian fault in the Sea of Marmara. Journal of Geophysical Research, 108, 2179.
716   https://doi.org/10.1029/2002JB001862
717 Le Pichon, X., Şengör, A. M. C., Demirbağ, E., Rangin, C., İmren, C., Armijo, R., Görür, N.,
718   Çağatay, N., Mercier de Lepinay, B., Meyer, B., Saatçılar, R., & Tok, B. (2001). The
719   active Main Marmara Fault. Earth and Planetary Science Letters, 192(4), 595–616.
720   https://doi.org/10.1016/S0012-821X(01)00449-6
721 Liu, J. T., Wang, Y.-H., Yang, R. J., Hsu, R. T., Kao, S.-J., Lin, H.-L., & Kuo, F. H. (2012).
722   Cyclone-induced hyperpycnal turbidity currents in a submarine canyon. Journal of
723   Geophysical Research: Oceans, 117(C4), n/a-n/a.
724   https://doi.org/10.1029/2011JC007630
725 McHugh, C. M. G., Seeber, L., Cormier, M. H., Dutton, J., Cagatay, N., Polonia, A., Ryan, W.
726   B. F., & Gorur, N. (2006). Submarine earthquake geology along the North Anatolia Fault
727   in the Marmara Sea, Turkey: A model for transform basin sedimentation. Earth and
728   Planetary Science Letters, 248, 661–684. https://doi.org/10.1016/j.epsl.2006.05.038
729 McHugh, C. M., Seeber, L., Braudy, N., Cormier, M. H., Davis, M. B., Diebold, J. B.,
730   Dieudonne, N., Douilly, R., Gulick, S. P. S., Hornbach, M. J., Johnson, H. E., Mishkin, K.

731   R., Sorlien, C. C., Steckler, M. S., Symithe, S. J., & Templeton, J. (2011). Offshore

732   sedimentary effects of the 12 January 2010 Haiti earthquake. Geology, 39(8), 723–726.

733   https://doi.org/10.1130/G31815.1

734 McHugh, C. M. G., Braudy, N., Çağatay, M. N., Sorlien, C., Cormier, M.-H., Seeber, L., &

735   Henry, P. (2014). Seafloor fault ruptures along the North Anatolia Fault in the Marmara

736   Sea, Turkey: Link with the adjacent basin turbidite record. Marine Geology, 353, 65–83.

737   https://doi.org/10.1016/j.margeo.2014.03.005

738 Mikada, H., Mitsuzawa, K., Matsumoto, H., Watanabe, T., Morita, S., Otsuka, R., Sugioka,

739   H., Baba, T., Araki, E., & Suyehiro, K. (2006). New discoveries in dynamics of an M8

740   earthquake-phenomena and their implications from the 2003 Tokachi-oki earthquake

741   using a long term monitoring cabled observatory. Tectonophysics, 426(1–2), 95–105.

742   https://doi.org/10.1016/j.tecto.2006.02.021

743 Mulder, T., & Cochonnat, P. (1996). Classification of Offshore Mass Movements. SEPM

744   Journal of Sedimentary Research, Vol. 66. https://doi.org/10.1306/D42682AC-2B26-

745   11D7-8648000102C1865D

746 Mulder, T., Syvitski, J. P. M., Migeon, S., Faugères, J.-C., & Savoye, B. (2003). Marine

747   hyperpycnal flows: initiation, behavior and related deposits. A review. Marine and

748   Petroleum Geology, 20(6–8), 861–882. https://doi.org/10.1016/j.marpetgeo.2003.01.003

749 Nakajima, T., & Kanai, Y. (2000). Sedimentary features of seismoturbidites triggered by the

750   1983 and older historical earthquakes in the eastern margin of the Japan Sea.

751   Sedimentary Geology, 135(1–4), 1–19. https://doi.org/10.1016/S0037-0738(00)00059-2

752 Normandeau, A., Bourgault, D., Neumeier, U., Lajeunesse, P., St-Onge, G., Gostiaux, L., &

753   Chavanne, C. (2020). Storm-induced turbidity currents on a sediment-starved shelf:

754   Insight from direct monitoring and repeat seabed mapping of upslope migrating

755   bedforms. Sedimentology, 67(2), 1045–1068. https://doi.org/10.1111/sed.12673

756 Okal, E. A., & Synolakis, C. E. (2001). Comment on "Origin of the 17 July 1998 Papua New

757   Guinea Tsunami: Earthquake or Landslide?" by E. L. Geist. Seismological Research

758   Letters, 72(3), 362–366. https://doi.org/10.1785/gssrl.72.3.362

759 Özeren, M. S., Çağatay, M. N., Postacioğlu, N., Şengör, a. M. C., Görür, N., & Eriş, K.

760   (2010). Mathematical modelling of a potential tsunami associated with a late glacial

761   submarine landslide in the Sea of Marmara. Geo-Marine Letters, 30, 523–539.

762   https://doi.org/10.1007/s00367-010-0191-1

763 Parker, G. (1982). Conditions for the ignition of catastrophically erosive turbidity currents.

764   Marine Geology, 46(3–4), 307–327. https://doi.org/10.1016/0025-3227(82)90086-X

765 Piper, D. J. W., & Normark, W. R. (2009). Processes That Initiate Turbidity Currents and

766   Their Influence on Turbidites: A Marine Geology Perspective. Journal of Sedimentary

767   Research, 79(6), 347–362. https://doi.org/10.2110/jsr.2009.046

768   Piper, D. J. W., Cochonat, P., & Morrison, M. L. (1999). The sequence of events around the
769   epicentre of the 1929 Grand Banks earthquake: initiation of debris flows and turbidity
770   current inferred from sidescan sonar. Sedimentology, 46(1), 79–97.
771   https://doi.org/10.1046/j.1365-3091.1999.00204.x
772   Polonia, A., Vaiani, S. C., & De Lange, G. J. (2016). Did the A.D. 365 Crete
773   earthquake/tsunami trigger synchronous giant turbidity currents in the Mediterranean
774   Sea? Geology, 44(3), 191–194. https://doi.org/10.1130/G37486.1
775   Pope, E. L., Talling, P. J., & Carter, L. (2017). Which earthquakes trigger damaging
776   submarine mass movements: Insights from a global record of submarine cable breaks?
777   Marine Geology, 384, 131–146. https://doi.org/10.1016/j.margeo.2016.01.009
778   Şengör, A. M. C., Grall, C., İmren, C., Le Pichon, X., Görür, N., Henry, P., Karabulut, H., &
779   Siyako, M. (2014). The geometry of the North Anatolian transform fault in the Sea of
780   Marmara and its temporal evolution: implications for the development of intracontinental
781   transform faults. Canadian Journal of Earth Sciences, 51(3), 222–242.
782   https://doi.org/10.1139/cjes-2013-0160
783   Synolakis, C. E., Bardet, J.-P., Borrero, J. C., Davies, H. L., Okal, E. A., Silver, E. A., Sweet,
784   S., & Tappin, D. R. (2002). The slump origin of the 1998 Papua New Guinea Tsunami.
785   Proceedings of the Royal Society of London. Series A: Mathematical, Physical and
786   Engineering Sciences, 458(2020), 763–789. https://doi.org/10.1098/rspa.2001.0915
787   Xu, J. P., Noble, M. A., & Rosenfeld, L. K. (2004). In-situ measurements of velocity structure
788   within turbidity currents. Geophysical Research Letters, 31(9).
789   https://doi.org/10.1029/2004GL019718
790   Xu, J. P., Swarzenski, P. W., Noble, M., & Li, A.-C. (2010). Event-driven sediment flux in
791   Hueneme and Mugu submarine canyons, southern California. Marine Geology, 269(1–
792   2), 74–88. https://doi.org/10.1016/j.margeo.2009.12.007
793   Yakupoğlu, N., Uçarkuş, G., Kadir Eriş, K., Henry, P., & Namık Çağatay, M. (2019).
794   Sedimentological and geochemical evidence for seismoturbidite generation in the
795   Kumburgaz Basin, Sea of Marmara: Implications for earthquake recurrence along the
796   Central High Segment of the North Anatolian Fault. Sedimentary Geology, 380, 31–44.
797   https://doi.org/10.1016/j.sedgeo.2018.11.002
798   Zitter, T. A. C., Grall, C., Henry, P., Özeren, M. S., Çağatay, M. N., Şengör, A. M. C.,
799   Gasperini, L., de Lépinay, B. M., & Géli, L. (2012). Distribution, morphology and triggers
800   of submarine mass wasting in the Sea of Marmara. Marine Geology, 329–331, 58–74.
801   https://doi.org/10.1016/j.margeo.2012.09.002